






Cite this: DOI: 10.1039/d0cy02471f

# Effect of FeO<sub>x</sub> and MnO<sub>x</sub> doping into the CeO<sub>2</sub>-V<sub>2</sub>O<sub>5</sub>/TiO<sub>2</sub> nanocomposite on the performance and mechanism in selective catalytic reduction of NO<sub>x</sub> with NH<sub>3</sub>†

Jinxiu Wang, <sup>a</sup> Xianfang Yi,<sup>ab</sup> Qingfa Su,<sup>ab</sup> Jinsheng Chen <sup>\*a</sup> and Zongli Xie <sup>\*c</sup>

Researchers have been working on the development of new low temperature catalysts with high NO<sub>x</sub> conversion, N<sub>2</sub> selectivity and resistance to SO<sub>2</sub> and H<sub>2</sub>O in selective catalytic reduction of NO<sub>x</sub> with NH<sub>3</sub> at 120–300 °C. Here, a series of novel FeO<sub>x</sub>-CeO<sub>2</sub>-V<sub>2</sub>O<sub>5</sub>/TiO<sub>2</sub> (FeCeVTi) and MnO<sub>x</sub>-CeO<sub>2</sub>-V<sub>2</sub>O<sub>5</sub>/TiO<sub>2</sub> (MnCeVTi) catalysts were synthesized *via* a modified solvent-free sol-gel method and their catalytic performances at low temperature were enhanced by doping different contents of Fe or Mn. Among them, the 7%FeCeVTi catalyst (7.0% Ce/Ti and 1.0% V/Ti molar ratio) showed the optimal integrated catalytic performance, whose NO<sub>x</sub> conversion remained above 92% between 210 and 360 °C and above 86.1% when introducing SO<sub>2</sub> for 24 h at 250 °C with nearly 100% N<sub>2</sub> selectivity. The interaction among Fe, Ce and V species in FeCeVTi catalysts contributed to their higher Ce<sup>3+</sup>/Ce<sup>4+</sup> and surface V<sup>5+</sup> ratio, appropriate redox ability, and more acid sites, which may result in the improvement of their SCR activity and resistance to SO<sub>2</sub>. The addition of MnO<sub>x</sub> into the CeVTi system increased the catalytic activity below 235 °C, but largely decreased the N<sub>2</sub> selectivity and did not enhance the resistance to SO<sub>2</sub> and H<sub>2</sub>O, which may be due to the too high redox ability of the MnCeVTi catalyst. The NH<sub>3</sub>-SCR reaction on the CeVTi sample followed the E-R mechanism, and the coexistence of E-R and L-H mechanisms was observed on the FeCeVTi catalyst.

Received 27th December 2020,  
Accepted 14th February 2021

DOI: 10.1039/d0cy02471f

rsc.li/catalysis

## 1. Introduction

Nitrogen oxides (NO<sub>x</sub>) are the major air pollutants causing acid rain, photochemical smog, ozone depletion and haze. The selective catalytic reduction of NO<sub>x</sub> with ammonia (NH<sub>3</sub>-SCR) technique as an effective technology is widely used in controlling NO<sub>x</sub> emission from stationary sources. Because the commercial V<sub>2</sub>O<sub>5</sub>-WO<sub>3</sub> (or MoO<sub>3</sub>)/TiO<sub>2</sub> catalyst is highly active and has good tolerance to SO<sub>2</sub> and H<sub>2</sub>O at the optimum working temperature of 300–400 °C, it has been widely used for the NH<sub>3</sub>-SCR of NO<sub>x</sub> in coal-fired plants. However, some other stationary sources require the removal of NO<sub>x</sub> at low temperatures (120–300 °C). Therefore, many researchers are devoting efforts to the development of new low temperature catalysts.<sup>1–4</sup>

Many efforts have been made to obtain low temperature catalysts with high NO<sub>x</sub> conversion, N<sub>2</sub> selectivity and resistance to SO<sub>2</sub> and H<sub>2</sub>O by modifying the V<sub>2</sub>O<sub>5</sub>/TiO<sub>2</sub> based catalyst with transition or rare earth metal oxides.<sup>5,6</sup> Among them, CeO<sub>2</sub>-added V<sub>2</sub>O<sub>5</sub>/TiO<sub>2</sub> catalysts exhibit high SCR activity in the presence of SO<sub>2</sub> and water vapor at 250–400 °C.<sup>7–14</sup> And, they are prepared commonly by impregnation, deposition precipitation and chemical vapor condensation methods. CeO<sub>2</sub> has good reducibility because it plays the role of oxygen storage, and the different oxidation states of Ce ions were attributed to different reactions during catalysis.<sup>11</sup> However, the CeO<sub>2</sub>-V<sub>2</sub>O<sub>5</sub>/TiO<sub>2</sub> catalyst is not active in SCR of NO<sub>x</sub> below 200 °C. Transition metal doping is considered an effective approach to further improve the catalytic performance at low temperature. MnO<sub>x</sub> and FeO<sub>x</sub>-based metal oxide catalysts have shown very high NH<sub>3</sub>-SCR activity at low-temperatures (<200 °C) in the absence of SO<sub>2</sub>/H<sub>2</sub>O in the feed stream. However, overcoming the deactivation and low N<sub>2</sub>-selectivity values is still a challenge.<sup>3,15–19</sup> The synergetic effect between Mn and Ce in increasing SCR catalytic activity and N<sub>2</sub> selectivity has been reported for Mn-Ce/TiO<sub>2</sub>,<sup>20</sup> Fe and Co doped Mn-Ce/TiO<sub>2</sub>,<sup>21</sup> Mn-Ce-Fe-Ti,<sup>22</sup> Mn/Ce/W/Ti (ref. 23) and so on. Cerium is capable of decreasing the

<sup>a</sup> Center for Excellence in Regional Atmospheric Environment, and Key Lab of Urban Environment and Health, Institute of Urban Environment, Chinese Academy of Sciences, Xiamen 361021, P.R. China. E-mail: jschen@iue.ac.cn

<sup>b</sup> University of Chinese Academy of Sciences, Beijing 100049, P.R. China

<sup>c</sup> CSIRO Manufacturing, Private bag 10, Clayton South MDC, VIC 3169, Australia

† Electronic supplementary information (ESI) available. See DOI: 10.1039/d0cy02471f

formation rate of sulfate species on the surface of Ce-modified Mn-based catalysts, thus promoting the tolerance to SO<sub>2</sub>.<sup>16</sup> The reported Mn–Ce–VO<sub>x</sub>/TiO<sub>2</sub> (ref. 24 and 25) and Mn–Ce–V–WO<sub>x</sub>/TiO<sub>2</sub> (ref. 26) catalysts furthermore indicate that the addition of Mn into the CeO<sub>2</sub>–V<sub>2</sub>O<sub>5</sub>/TiO<sub>2</sub> system may be a useful method to enhance NO<sub>x</sub> conversion at low temperature.

The effect of Fe doping on the low temperature deNO<sub>x</sub> activity of V<sub>2</sub>O<sub>5</sub>/TiO<sub>2</sub> nanoparticles has also been studied. Schill *et al.* reported that doping V(0.17)/TiO<sub>2</sub> with a small amount of Fe(0.03) can significantly alter its surface and redox properties but does not increase the activity of the V(0.17)/TiO<sub>2</sub> catalyst and can, depending on the method of Fe introduction, cause strong deactivation at 150 to 200 °C and in the presence of 20 vol% H<sub>2</sub>O.<sup>27</sup> Zhu *et al.* reported that Fe<sub>0.1</sub>V<sub>0.1</sub>TiO<sub>x</sub> achieves >90% NO<sub>x</sub> conversion at 225–450 °C under a GHSV of 200 000 h<sup>-1</sup> and maintains NO<sub>x</sub> conversion above 93% at 250 °C after introducing SO<sub>2</sub> and H<sub>2</sub>O for 24 h. The charge interaction between Fe<sub>2</sub>O<sub>3</sub> and FeVO<sub>4</sub> as well as the electronic inductive effect between Fe and V species results in the improvement of SCR activity and N<sub>2</sub> selectivity at high temperatures.<sup>28</sup> Nevertheless, the addition of both Fe and Ce into the V<sub>2</sub>O<sub>5</sub>/TiO<sub>2</sub> catalyst has not been studied. In view of these works, it is hypothesized that it may be probable to improve the SCR activity of CeO<sub>2</sub>–V<sub>2</sub>O<sub>5</sub>/TiO<sub>2</sub> at low temperature by doping FeO<sub>x</sub> or MnO<sub>x</sub> and meaningful to systematically compare the different roles of Fe and Mn in the CeO<sub>2</sub>–V<sub>2</sub>O<sub>5</sub>/TiO<sub>2</sub> system.

In this work, a series of FeO<sub>x</sub>–CeO<sub>2</sub>–V<sub>2</sub>O<sub>5</sub>/TiO<sub>2</sub> and MnO<sub>x</sub>–CeO<sub>2</sub>–V<sub>2</sub>O<sub>5</sub>/TiO<sub>2</sub> catalysts for SCR of NO<sub>x</sub> at low temperature were synthesized *via* a modified solvent-free sol–gel method and their catalytic performances were tuned by doping different contents of Fe or Mn. They were compared in terms of NH<sub>3</sub>–SCR activity, N<sub>2</sub> selectivity and resistance to H<sub>2</sub>O and SO<sub>2</sub>. The changes in their chemical and physical properties after the addition of Fe or Mn were systematically characterized and analyzed. The interaction of Fe (or Mn), Ce and V oxides and the reaction mechanism were further explored.

## 2. Experimental

### 2.1 Preparation of samples

The catalysts were synthesized by a modified solvent-free sol–gel method. Briefly, 0.1 mol of Ti(OC<sub>4</sub>H<sub>9</sub>)<sub>4</sub> was firstly dripped slowly into 360 mL of 0.5 mol L<sup>-1</sup> HNO<sub>3</sub> solution and then peptized and concentrated with constant stirring for 1 h to form a TiO<sub>2</sub> colloidal solution. NH<sub>4</sub>VO<sub>4</sub> and Ce(NO<sub>3</sub>)<sub>3</sub>·6H<sub>2</sub>O were then added into the TiO<sub>2</sub> sol and stirred for 1 h. Following that, Fe(NO<sub>3</sub>)<sub>3</sub>·9H<sub>2</sub>O or Mn(NO<sub>3</sub>)<sub>2</sub> was added into the above sol and then stirred for 16 h. The resulting sol was dried into a gel in a microwave oven and the gel was further dried using an electrothermal blowing dry box at 120 °C for 12 h. Finally, the precursor was calcined at 500 °C for 3 h at a ramping rate of 2 °C min<sup>-1</sup> in a tube furnace with 0.2 L min<sup>-1</sup> air flow to obtain x%FeCeVTi and x%MnCeVTi

catalysts. x% (3%, 7%, 10%) represents the molar ratio of Fe/Ti and Mn/Ti. The molar ratios of Ce/Ti and V/Ti of all the samples were kept constant at 7.0% and 1.0%, respectively.

### 2.2 Catalytic activity test

The catalytic activity of the samples was evaluated using a lab testing apparatus consisting of gas supply, a mixing gas section, a quartz tube fixed-bed reactor (diameter  $\phi$  6.0 mm) and an analyzer. All the samples were passed through a stainless steel sieve to obtain uniform size which was 0.28–0.45 mm. The samples were placed in the middle of the tube and sealed with quartz wool. The total volume flow rate was 500 mL min<sup>-1</sup> and the reaction feed gas composition consisted of 500 ppm NO<sub>x</sub> (~493 ppm NO and 7 ppm NO<sub>2</sub>), 500 ppm NH<sub>3</sub>, 5 vol% O<sub>2</sub>, 50 ppm SO<sub>2</sub> (when used), 3 vol% H<sub>2</sub>O (when used) and N<sub>2</sub> as balance gas. The concentrations of NO, NO<sub>2</sub>, N<sub>2</sub>O, NH<sub>3</sub> and SO<sub>2</sub> were determined using a Fourier transform infrared (FTIR) gas analyzer (Antaris IGS, Thermo Fisher Scientific). The activity test was conducted under two kinds of gas hourly space velocities (GHSVs). Under a GHSV of 50 000 h<sup>-1</sup>, 0.6 mL (0.745 g) of catalyst was loaded into the reactor. The test process was as follows. The samples were firstly tested without SO<sub>2</sub> and H<sub>2</sub>O at different temperatures (test 1) and then with H<sub>2</sub>O (test 2) and SO<sub>2</sub> (test 3) separately at 250 °C, and then underwent test 1 again (test 4). The used samples continued to be tested with both SO<sub>2</sub> and H<sub>2</sub>O (test 5) and then underwent test 1 again (test 6). Under a GHSV of 150 000 h<sup>-1</sup>, 0.2 mL (0.25 g) of catalyst was loaded and tested without H<sub>2</sub>O and with H<sub>2</sub>O at 180 °C and 250 °C.

The NO<sub>x</sub> conversion, N<sub>2</sub> selectivity and  $\Delta$ NH<sub>3</sub>/ $\Delta$ NO<sub>x</sub> were calculated using the following expressions:

$$\text{NO}_x \text{ conversion} = (1 - [\text{NO}_x]_{\text{out}}/[\text{NO}_x]_{\text{in}}) \times 100\%$$

$$\text{N}_2 \text{ selectivity} = (1 - 2[\text{N}_2\text{O}]_{\text{out}}/([\text{NO}_x]_{\text{in}} + [\text{NH}_3]_{\text{in}} - [\text{NO}_x]_{\text{out}} - [\text{NH}_3]_{\text{out}})) \times 100\%$$

$$\Delta\text{NH}_3/\Delta\text{NO}_x = ([\text{NH}_3]_{\text{in}} - [\text{NH}_3]_{\text{out}})/([\text{NO}_x]_{\text{in}} - [\text{NO}_x]_{\text{out}})$$

in which [NO<sub>x</sub>]<sub>in</sub>, [NO<sub>x</sub>]<sub>out</sub>, [NH<sub>3</sub>]<sub>in</sub>, [NH<sub>3</sub>]<sub>out</sub> and [N<sub>2</sub>O]<sub>out</sub> correspond to the inlet and outlet gas concentration, respectively. [NO<sub>x</sub>] means the total concentration of NO and NO<sub>2</sub>.

### 2.3 Characterization

Powder X-ray diffraction (XRD) patterns were collected with an X'Pert Pro (PANalytical B.V., Holland) and Cu K $\alpha$  rays at 40 kV and 40 mA were used to analyze the crystalline phase. Raman spectra were recorded with a LabRAM Aramis Raman spectrometer (Horiba Jobin Yvon S.A.S., France) using a 532 nm laser beam. The specific surface area was determined by N<sub>2</sub> adsorption at 77 K with the Brunauer–Emmett–Teller

(BET) method using a Nova 2000e analyzer (Quantachrome Corp., USA). Pore size distribution measurements were obtained from the  $N_2$  adsorption–desorption isotherm at 77 K. The morphology and elemental analysis of catalysts were obtained using a scanning electron microscope-energy dispersive spectrometer (SEM-EDS, S-4800, Hitachi and 51-ADD0009, Horiba, Japan). X-ray photoelectron spectroscopy (XPS) was conducted on an AXIS Supra (Kratos Analytical Inc.) with monochromatic Al  $K\alpha$  radiation ( $E = 1486.6$  eV, 150 W) as the X-ray source. Narrow region scans were acquired using a pass energy of 40 eV and a 0.1 eV step size and all spectra were calibrated with C 1s (284.8 eV). The temperature programmed desorption of  $NH_3$  and NO ( $NH_3$ -TPD and NO-TPD) and temperature programmed reduction of  $H_2$  ( $H_2$ -TPR) experiments were conducted on a ChemBET-3000 TPR-TPD chemisorption analyzer (Quantachrome, USA). The outlet gases were analyzed with an online mass spectrometer (MS, DYCOR LC-D200, Ametek Company, USA). Before the TPD test, each sample was pretreated in high-purity Ar flow at 500 °C for 1 h and cooled to room temperature. 100 mg of sample was exposed to 5%  $NH_3$  or 1% NO for 30 min and subsequently purged with Ar flow at 100 °C for 45 min to remove weakly adsorbed  $NH_3$  or NO on the surface. Then, the sample was heated to 600 °C at a ramping rate of 10 °C  $min^{-1}$  in Ar flow. In the TPR test, 50 mg of sample was loaded into a U-type quartz reactor and then heated at 500 °C for 1 h and then cooled down to room temperature in Ar flow. After that, the sample was heated to 900 °C at a rate of 10 °C  $min^{-1}$  in 5%  $H_2$ /Ar flow and the change of  $H_2$  ( $m/z = 2$ ) was recorded in the process.

*In situ* diffuse reflectance infrared Fourier transform spectroscopy (*in situ* DRIFTS) measurements were carried out with a Bruker Vertex 70 infrared spectrometer (Bruker, Germany) with a mercury–cadmium–telluride (MCT) detector and diffuse reflectance accessory (Harrick Scientific Products Inc) with ZnSe windows, a temperature controlling system and a reaction gas feed system. The experimental procedures were as follows. First, each sample was pretreated at 400 °C for 1 h and then cooled to the target temperature in a  $N_2$  atmosphere and the background spectrum was recorded. Then, the probe gas was introduced into the reaction chamber and the spectra were recorded at a resolution of 4  $cm^{-1}$  with 64 scans at set time. The obtained spectra with the background spectrum automatically subtracted were transformed into absorption spectra using the Kubelka–Munk function.

### 3. Results and discussion

#### 3.1 SCR catalytic activity

**3.1.1  $NO_x$  conversion and  $N_2$  selectivity.** Fig. 1 shows the  $NO_x$  conversion and  $N_2$  selectivity of the prepared samples. The CeVTi sample showed nearly 98%  $NO_x$  conversion in the higher temperature range of 235–365 °C. But the  $NO_x$  conversion of the CeVTi sample fell sharply with decreasing temperature and it was 87.6% at 212 °C and 57.5% at 188 °C. As the Fe content increased, the  $NO_x$  conversions of FeCeVTi

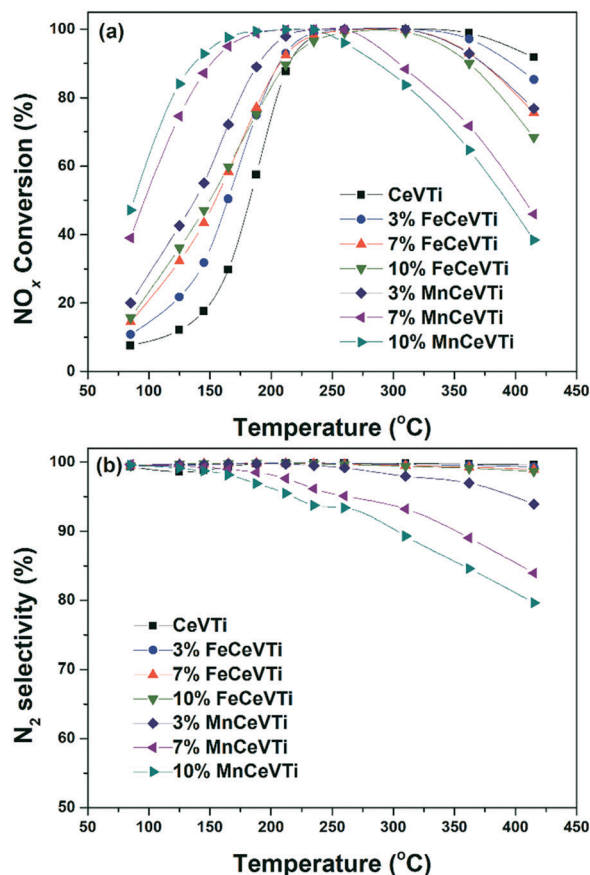


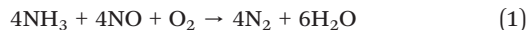
Fig. 1 (a)  $NO_x$  conversion and (b)  $N_2$  selectivity of the prepared samples measured at different temperatures with a gaseous mixture containing 500 ppm NO, 500 ppm  $NH_3$ , 5%  $O_2$  and  $N_2$  balance.

samples gradually increased below 188 °C and when the Fe content increased from 7% to 10%, the rate of change in  $NO_x$  conversion decreased, and so the 7%FeCeVTi sample was the optimal sample in consideration of economic cost. The  $NO_x$  conversions of 7%FeCeVTi reached 92.4% at 212 °C and 77.1% at 188 °C. The  $NO_x$  conversions of FeCeVTi samples remained above 98% between 235 and 310 °C and decreased with the Fe content above 310 °C. For MnCeVTi samples, their  $NO_x$  conversions gradually increased below 235 °C and decreased above 235 °C with increasing Mn content. The  $NO_2$  production also increased with the Mn content and temperature above 235 °C (shown in Fig. S1a†), which was one reason for the decrease in  $NO_x$  conversions of MnCeVTi samples at high temperature. The  $NO_x$  conversion of FeCeVTi samples was higher than that of MnCeVTi samples above 235 °C, and it was in reverse sequence below 235 °C. The coexistence of cerium oxide ( $CeO_x$ ) and vanadium oxide ( $VO_x$ ) played an important role in the SCR catalytic activity at temperatures above 235 °C. The presence of iron oxide ( $FeO_x$ ) improved the catalytic activity below 310 °C and the presence of manganese oxide ( $MnO_x$ ) enhanced it below 235 °C and inhibited it above 235 °C.

As shown in Fig. 1b, CeVTi and FeCeVTi samples showed nearly 100%  $N_2$  selectivity in the testing temperature range.

The  $N_2$  selectivity of MnCeVTi samples decreased with increasing Mn content and temperature and the corresponding  $N_2O$  production is shown in Fig. S1b.† The addition of Fe had little effect on  $N_2$  selectivity but the addition of Mn had a large adverse effect on it.

The desired reaction stoichiometry under typical SCR conditions is the following:



Under typical SCR conditions and over SCR metal oxide catalysts, the reaction between NO and  $NH_3$  can also proceed in a different way, giving rise to the unwanted product  $N_2O$ .  $N_2O$  mainly arises from  $NH_3 + NO$  (reaction (2)) and  $NH_3$  oxidation (reaction (3)).<sup>1</sup>



According to reactions (1) and (2), the consumption ratio of  $NH_3$  and NO is 1. However, once reaction (3) occurs, the consumption ratio of  $NH_3$  and NO will be higher than 1. In other words, a ratio of converted  $\Delta NH_3/\Delta NO_x > 1$  indicates that some ammonia is directly oxidized; the higher the ratio, the more ammonia being oxidized.

As shown in Fig. S1c,† for FeCeVTi samples, the  $NH_3$  oxidation reaction resulted in a little  $N_2O$  production above 350 °C. For MnCeVTi samples, both reactions (2) and (3) contributed to  $N_2O$  formation and the  $NH_3$  oxidation reaction began to play a role from 260 °C.<sup>24</sup>

**3.1.2 Effect of  $H_2O$ ,  $SO_2$  and their combination on SCR catalytic activity.** The effects of  $H_2O$ ,  $SO_2$  and their coexistence on the SCR catalytic activity of CeVTi, 7%FeCeVTi and 7%MnCeVTi samples were investigated and the results are displayed in Fig. 2. The  $NO_x$  conversions of CeVTi,

7%FeCeVTi and 7%MnCeVTi samples decreased only slightly from 99.3%, 98.7%, and 95.3% to 95.1%, 93.9%, and 94.4%, respectively, after the introduction of  $H_2O$  and kept constant for 12 h and then recovered to 98.3%, 97.8%, and 93.7% after  $H_2O$  was turned off for about 1.5 h at 250 °C. The three catalysts maintained above 94% conversion in the presence of  $H_2O$  and the difference in  $NO_x$  conversions is small at 250 °C with a GHSV of 50 000  $h^{-1}$ . In order to further study the effect of  $H_2O$ , experiments with a lower catalyst amount (0.25 g) corresponding to a GHSV of 150 000  $h^{-1}$  were performed both at 180 °C and 250 °C, and the results are shown in Fig. S2.† The  $NO_x$  conversions of CeVTi, 7%FeCeVTi and 7%MnCeVTi catalysts decreased from 73.8%, 73.2%, and 87.4% to 62.3%, 59.5%, and 68.6%, respectively, after the introduction of  $H_2O$  and then recovered to 73.3%, 72.1%, and 84.3% after  $H_2O$  was turned off at 250 °C with a GHSV of 150 000  $h^{-1}$ . CeVTi and 7%FeCeVTi catalysts maintained nearly 100%  $N_2$  selectivity all the time. The  $NO_x$  conversion of 7%MnCeVTi was highest, which was partly contributed by the lowest  $N_2$  selectivity (87.5%). The  $N_2$  selectivity of the 7%MnCeVTi catalyst increased to 99.0% in the presence of  $H_2O$ .  $N_2O$  formation during the low temperature SCR reaction over manganese oxide-based catalysts was obviously inhibited by  $H_2O$ .<sup>29,30</sup> In the reaction at 180 °C with a GHSV of 150 000  $h^{-1}$ , the  $NO_x$  conversions of CeVTi, 7%FeCeVTi and 7%MnCeVTi catalysts changed from 21.4%, 33.5%, and 54.9% to 22.2%, 27.2%, and 36.5%, respectively, after the introduction of  $H_2O$  and then recovered to 19.6%, 35.2%, and 54.9% after  $H_2O$  was turned off. After the introduction of  $H_2O$ , the  $NO_x$  conversions of 7%FeCeVTi and 7%MnCeVTi catalysts decreased by 6.3% and 18.4% at 180 °C, respectively. The addition of  $MnO_x$  induced a higher reduction of  $H_2O$  resistance of the CeVTi catalyst than the addition of  $FeO_x$  at 180 °C with a GHSV of 150 000  $h^{-1}$ .

On the other hand, the SCR performance of these three catalysts differed differently when  $SO_2$  was introduced into the feed. As shown in Fig. 2, the  $NO_x$  conversions of CeVTi, 7%FeCeVTi and 7%MnCeVTi samples at 250 °C decreased to 56.3%, 86.1% and 56.9% after introducing  $SO_2$  for about 24 h and could not recover when  $SO_2$  was removed from the feed stream. The  $FeO_x$  doped catalyst 7%FeCeVTi had the highest resistance to  $SO_2$ . The samples continued to be tested in the presence of both  $SO_2$  and  $H_2O$ . The  $NO_x$  conversions of CeVTi, 7%FeCeVTi and 7%MnCeVTi samples at 250 °C decreased to 30.2%, 58.0%, and 29.6% after introducing  $SO_2$  and  $H_2O$  for 24 h and recovered to 49.8%, 83.0%, and 51.2% when  $SO_2$  and  $H_2O$  were removed from the feed stream. Therefore, 7%FeCeVTi had the highest resistance to  $SO_2$  and  $H_2O$ .

As shown in Fig. S3,† the  $NO_x$  conversions measured at different temperatures for the used sample after the  $SO_2$  resistance test (test 4, suffix-S) and those after the following  $SO_2$ - $H_2O$  resistance test (test 6, suffix-SH) were similar. It indicates that the samples were poisoned in the  $SO_2$  resistance test and not further poisoned by the combination of  $SO_2$  and  $H_2O$ . After the test of resistance to  $SO_2$  and  $H_2O$ , the  $NO_x$

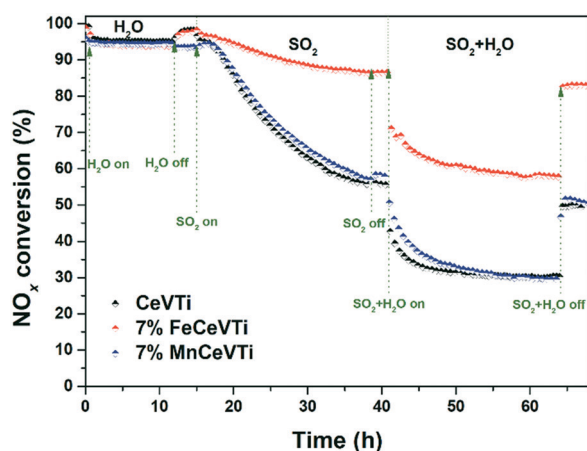


Fig. 2 The effect of  $H_2O$ ,  $SO_2$ ,  $H_2O$  and  $SO_2$  on  $NO_x$  conversion of CeVTi, 7%FeCeVTi and 7%MnCeVTi with time at 250 °C in the reaction gas containing 500 ppm NO, 500 ppm  $NH_3$ , 5 vol%  $O_2$ , 50 ppm  $SO_2$  (when used), 3 vol%  $H_2O$  (when used) and  $N_2$  balance.

conversion of the used 7%FeCeVTi sample was highest below 375 °C and remained nearly 100% at 275–375 °C.

### 3.2 Composition and structure

**3.2.1 XRD patterns and Raman spectra.** The effect of iron oxide or manganese oxide loading on the crystal phases of the prepared catalysts was investigated using XRD. As shown in Fig. 3, the detected peaks corresponded to the polymorphic form of TiO<sub>2</sub> including anatase (PDF 01-073-1764) as the main crystal phase, rutile (PDF 01-073-1765) and brookite (PDF 01-076-1934) for all the samples. No diffraction peaks attributable to FeO<sub>x</sub>, MnO<sub>x</sub>, CeO<sub>x</sub> and VO<sub>x</sub> were detected, which implied that they were present in low crystallinity phases and/or the content was below the detection limit of XRD. As the amount of Fe increased in FeCeVTi samples, the intensities of anatase diffraction peaks gradually decreased and the full width at half maximum (FWHM) of the anatase diffraction peaks increased. That is to say, the addition of Fe can obviously decrease the crystalline degree and grain size of TiO<sub>2</sub> in FeCeVTi samples. The anatase diffraction peaks in MnCeVTi samples changed little with increasing Mn. Moreover, the presence of Fe inhibited the growth of rutile and brookite more obviously than Mn. Therefore, the effect of FeO<sub>x</sub> loading on the crystal phases of the prepared catalysts was larger than that of MnO<sub>x</sub>.

As shown in Fig. 4, the Raman spectra of CeVTi, 7%FeCeVTi and 7%MnCeVTi showed weak bands of nanocrystalline V<sub>2</sub>O<sub>5</sub> at 195 and 255 cm<sup>-1</sup> in addition to the typical bands of CeO<sub>2</sub> at 448 cm<sup>-1</sup> and anatase TiO<sub>2</sub> at 148, 399, 521 and 613 cm<sup>-1</sup>, respectively.<sup>31</sup> The bands at 691 cm<sup>-1</sup> and 800 cm<sup>-1</sup> were attributed to the Mn–O single bond vibration of MnO<sub>2</sub> and characteristic of FeVO<sub>x</sub>, respectively.<sup>28,32</sup> For 7%FeCeVTi and 7%MnCeVTi, the intensity of TiO<sub>2</sub> Raman peaks decreased due to the coverage of the TiO<sub>2</sub> surface by FeO<sub>x</sub> or MnO<sub>x</sub>.

**3.2.2 BET specific surface area and pore volume.** Fig. 5 shows the nitrogen adsorption–desorption isotherms of the prepared samples and the analysis results of Fig. 5 are shown

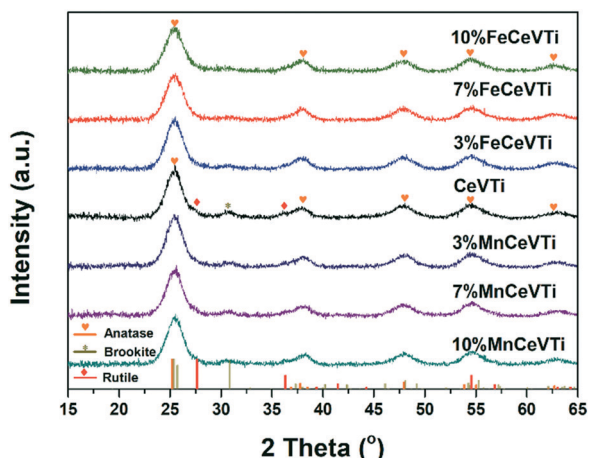


Fig. 3 XRD patterns of the prepared catalysts.

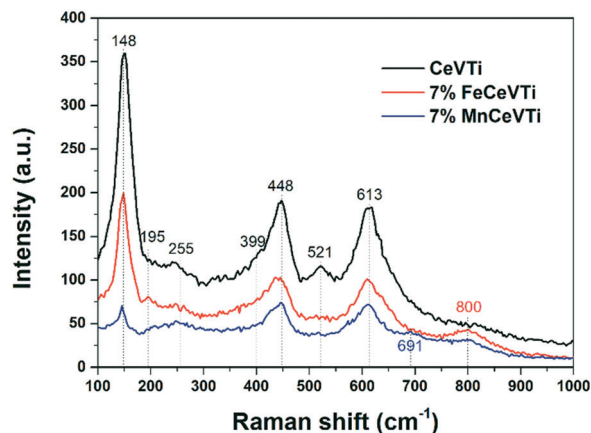


Fig. 4 Raman spectra of CeVTi, 7%FeCeVTi and 7%MnCeVTi catalysts.

in Table 1 including the BET specific surface area ( $S_{\text{BET}}$ ), pore volume ( $V_{\text{p}}$ ) and average pore diameter ( $D_{\text{A}}$ ) of the samples. The N<sub>2</sub>-adsorption isotherm of these samples belongs to the type-IV isotherm and their  $D_{\text{A}}$  is in the range of 4.4–4.7 nm, so the prepared samples are mesoporous materials.<sup>33</sup> The increase in  $S_{\text{BET}}$  and  $V_{\text{p}}$  values of FeCeVTi samples was observed upon increasing the Fe content. But for MnCeVTi

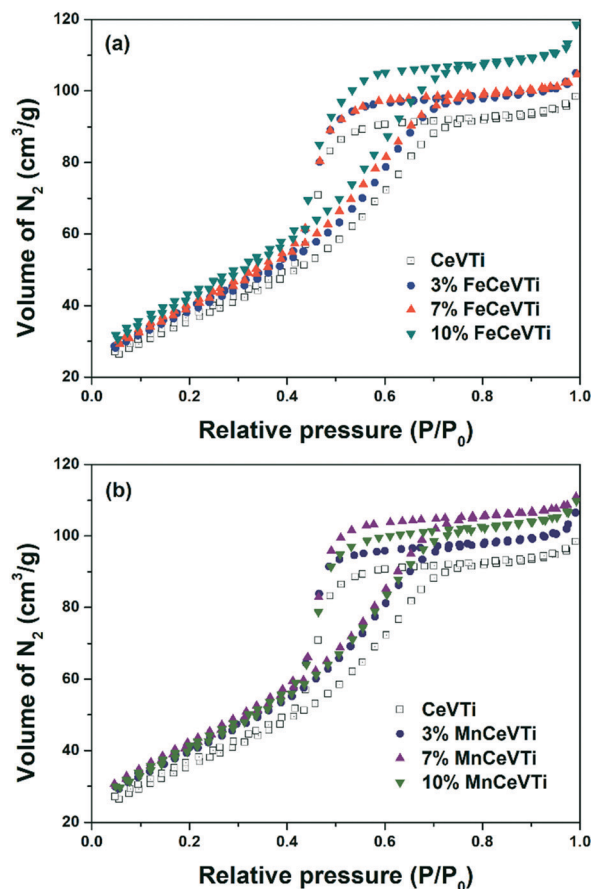


Fig. 5 Nitrogen adsorption–desorption isotherms of the prepared (a) FeCeVTi and (b) MnCeVTi catalysts.

**Table 1** BET specific surface area, pore volume and average pore diameter of the prepared catalysts

| Sample     | $S_{\text{BET}}$ ( $\text{m}^2 \text{g}^{-1}$ ) | $V_{\text{P}}$ ( $\text{cm}^3 \text{g}^{-1}$ ) | $D_{\text{A}}$ (nm) |
|------------|---|--|---------------------|
| CeVTi      | 132   | 0.15   | 4.6                 |
| 3%FeCeVTi  | 142   | 0.16   | 4.6                 |
| 7%FeCeVTi  | 147   | 0.16   | 4.4                 |
| 10%FeCeVTi | 156   | 0.18   | 4.7                 |
| 3%MnCeVTi  | 147   | 0.16   | 4.5                 |
| 7%MnCeVTi  | 153   | 0.17   | 4.5                 |
| 10%MnCeVTi | 150   | 0.17   | 4.5                 |

samples, the  $S_{\text{BET}}$  and  $V_{\text{P}}$  values increased upon increasing the Mn content lower than 7%, and then began to decrease. The  $D_{\text{A}}$  values were not significantly affected by Fe or Mn addition. The trend of  $S_{\text{BET}}$  and  $V_{\text{P}}$  values correlated well with the crystallinity of the samples. Fe had a larger effect than Mn on optimizing the structure of the prepared catalyst samples. It may be concluded that Fe doping inhibited the crystal growth of  $\text{TiO}_2$ , and consequently helped to increase the surface areas and pore volumes, which is beneficial to the SCR catalytic activity.<sup>34</sup>

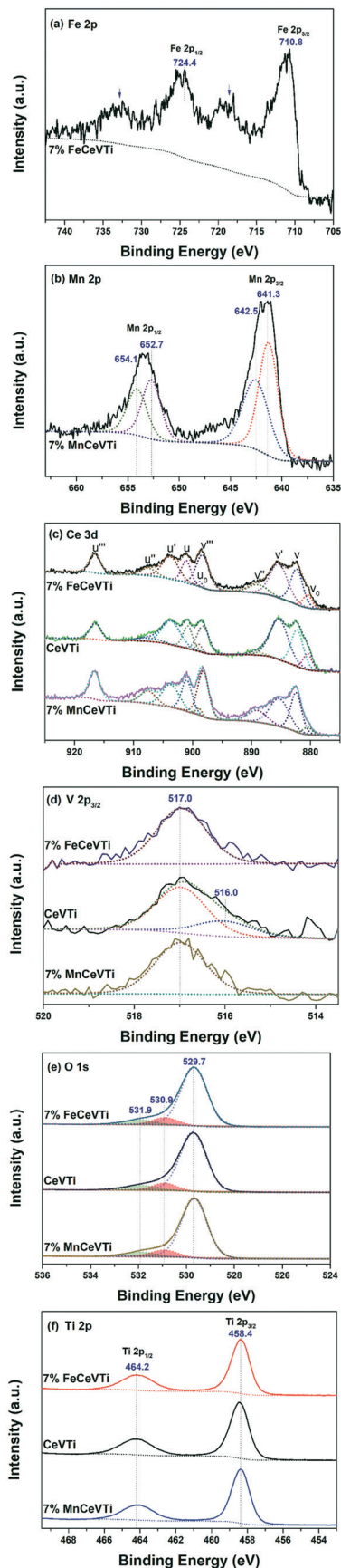
**3.2.3 Morphology and element analysis.** SEM images of CeVTi, 7%FeCeVTi and 7%MnCeVTi are shown in Fig. S4†. Overall, the morphologies of all three catalysts, in particular 7%FeCeVTi and 7%MnCeVTi, were similar. All the catalysts were composed of fine nanoparticles and no obvious phase separation could be observed. Compared with the CeVTi catalyst, 7%FeCeVTi and 7%MnCeVTi possessed smaller nanoparticle size. Fig. S5† shows the EDS-mapping images of elements in the 7%FeCeVTi catalyst, confirming the uniform distribution of Fe, Ce, V and Ti elements. According to the results of EDS, the mean atomic ratio of Ce/Ti and V/Ti in all the samples was 7.40% and 2.28%, respectively. The atomic ratio of Fe/Ti in FeCeVTi samples and Mn/Ti in MnCeVTi samples increased in proportion to the design value (Table 2). S deposition was detected on the used samples after the test of resistance to  $\text{SO}_2$  and  $\text{H}_2\text{O}$ . Used 7%FeCeVTi had lower S deposition (1.27% S/Ti) than used 7%MnCeVTi (2.83% S/Ti), and the order was consistent with the result of the resistance test.

### 3.3 Surface chemical properties

**3.3.1 XPS analysis.** Fig. 6 shows the Fe 2p, Mn 2p, Ce 3d, V 2p, O 1s and Ti 2p XPS spectra of CeVTi, 7%FeCeVTi, and 7%MnCeVTi catalysts. The Fe 2p spectra (Fig. 6a) show that

**Table 2** Atomic ratio (%) from EDS results of the prepared catalysts

| Sample     | Fe/Ti (%) | Mn/Ti (%) |
|------------|-----------|-----------|
| 3%FeCeVTi  | 3.59      | —         |
| 7%FeCeVTi  | 9.24      | —         |
| 10%FeCeVTi | 12.18     | —         |
| 3%MnCeVTi  | —         | 3.92      |
| 7%MnCeVTi  | —         | 8.88      |
| 10%MnCeVTi | —         | 11.99     |

**Fig. 6** (a) Fe 2p, (b) Mn 2p, (c) Ce 3d, (d) V 2p, (e) O 1s and (f) Ti 2p XPS spectra of 7%FeCeVTi, CeVTi and 7%MnCeVTi catalysts.

**Table 3** Surface atomic ratios (%) from XPS over samples

| Samples   | Ce <sup>3+</sup> /Ce <sup>4+</sup> | O <sub>β</sub> /O <sub>α</sub> | O <sub>γ</sub> /O <sub>α</sub> | Fe/Ti | Mn/Ti | Ce/Ti | V/Ti |
|-----------|------------------------------------|--------------------------------|--------------------------------|-------|-------|-------|------|
| CeVTi     | 95.0                               | 10.6                           | 8.8                            | —     | —     | 6.3   | 2.2  |
| 7%FeCeVTi | 71.2                               | 11.3                           | 8.4                            | 8.8   | —     | 7.2   | 2.2  |
| 7%MnCeVTi | 51.7                               | 10.8                           | 8.1                            | —     | 7.5   | 8.3   | 2.0  |

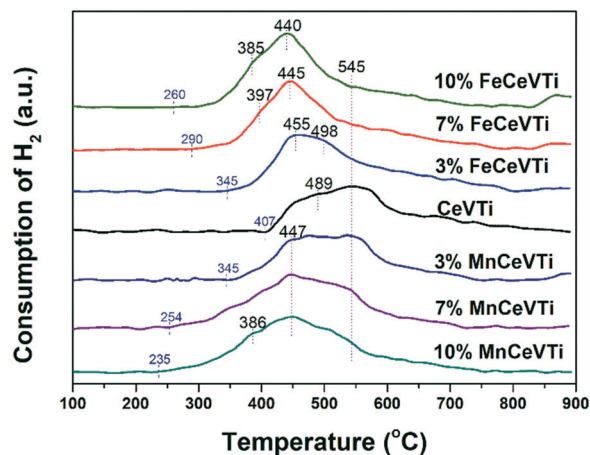
two peaks at 710.8 eV and 724.4 eV and satellite peaks (indicated by an arrow) were clearly observed on the 7%FeCeVTi catalyst which could be assigned to 2p<sub>3/2</sub> and 2p<sub>1/2</sub> of Fe<sup>3+</sup>.<sup>35</sup> The Mn 2p spectra (Fig. 6b) show two observed peaks attributed to Mn 2p<sub>3/2</sub> and Mn 2p<sub>1/2</sub> in the 7%MnCeVTi catalyst which were further deconvoluted and assigned to Mn<sup>3+</sup> (641.3 and 652.7 eV) and Mn<sup>4+</sup> (642.5 and 654.1 eV), respectively.<sup>36,37</sup> The ratio of Mn<sup>3+</sup>/Mn<sup>4+</sup> was 1.2 in the 7%MnCeVTi catalyst.

The CeO<sub>2</sub> spectrum is composed of two multiplets (v and u) which respectively correspond to the spin-orbit split 3d<sub>5/2</sub> and 3d<sub>3/2</sub> core holes. As shown in Fig. 6c, the Ce 3d XPS spectra can be deconvoluted into ten peaks. The peaks labeled as u<sup>m</sup> (916.5 eV), v<sup>m</sup> (898.2 eV), u<sup>n</sup> (907.5 eV), v<sup>n</sup> (888.9 eV), u (901 eV) and v (882.3 eV) are assigned to Ce<sup>4+</sup>. The peaks labeled as u<sub>0</sub> (898.9 eV), v<sub>0</sub> (880.5 eV), u' (903.7 eV) and v' (885.3 eV) are associated with Ce<sup>3+</sup>.<sup>38,39</sup> In the CeVTi sample, the ratio of Ce<sup>3+</sup>/Ce<sup>4+</sup> was nearly 1:1, and the addition of Fe or Mn decreased the ratio of Ce<sup>3+</sup>/Ce<sup>4+</sup>. This was because electrons are easy to transfer from Ce<sup>3+</sup> to oxygen or Fe or Mn species during the preparation process.<sup>40</sup> With Ce<sup>3+</sup> as a reactive species, a higher proportion of Ce<sup>3+</sup> could form more oxygen vacancies, which is conducive to the SCR reaction process.<sup>41</sup> The sequence of the Ce<sup>3+</sup>/Ce<sup>4+</sup> ratio in the three catalysts was in accordance with that of the SCR catalytic activity in the temperature range above 235 °C. As shown in Fig. 6d, the V 2p<sub>3/2</sub> spectra of the CeVTi sample were fitted into two peaks at 517.0 eV and 516.0 eV, corresponding to V<sup>5+</sup> and V<sup>4+</sup> of vanadium oxide.<sup>42</sup> Only the peak of V<sup>5+</sup> was observed on 7%FeCeVTi and 7%MnCeVTi catalysts. Previous studies verified that a strong electronic inductive effect exists between Fe<sup>3+</sup> and V<sup>5+</sup> species, which is beneficial to the improvement of SCR activity and N<sub>2</sub> selectivity at high temperatures.<sup>28,43</sup> The introduction of Fe (or Mn) affected the valence of Ce and V, which indicated there was an interaction between Fe (or Mn), Ce and V.<sup>10,25</sup>

The O 1s spectra of the samples (Fig. 6e) have been resolved into three peaks assigned to the lattice oxygen (O<sub>α</sub>) of the metal oxides at 529.7 eV, surface hydroxyl (-OH) groups (O<sub>β</sub>) at 530.9 eV and weakly adsorbed oxygen (O<sub>γ</sub>) at 531.9 eV, respectively.<sup>44,45</sup> As listed in Table 3, the three samples had similar ratios of surface chemisorbed oxygen (O<sub>β</sub> + O<sub>γ</sub>) which is highly active in reactions because of its higher mobility than lattice oxygen.<sup>46,47</sup> The 7%FeCeVTi sample had the highest ratio of surface chemisorbed oxygen and then maybe the most abundant surface OH groups as Brønsted acid sites for NH<sub>3</sub> adsorption to supply sufficient reductant on the catalyst surface for NO<sub>x</sub> reduction in the SCR reaction.<sup>48</sup>

As displayed in Fig. 6f, the peaks at 464.2 eV and 458.4 eV are attributed to Ti 2p<sub>1/2</sub> and Ti 2p<sub>3/2</sub> characteristic peaks of Ti<sup>4+</sup>,<sup>49</sup> which were very similar in all three samples, indicating that there was no strong interaction between Fe (or Mn) and Ti. As displayed in Table 3, Fe/Ti, Mn/Ti, Ce/Ti and V/Ti semi-quantitative surface atomic ratios approximated the design values, which was in accordance with EDS results.

**3.3.2 Redox properties.** The NH<sub>3</sub>-SCR reaction usually requires a redox cycle of active sites in SCR catalysts to activate the reactants efficiently. Low redox ability will result in low deNO<sub>x</sub> efficiency, while too high redox ability may lead to unselective oxidation of NH<sub>3</sub> thus resulting in the lack of reducing agents and poor N<sub>2</sub> selectivity.<sup>48</sup> H<sub>2</sub>-TPR is widely employed to investigate the redox properties of SCR catalysts. The H<sub>2</sub>-TPR profiles of the prepared samples are presented in Fig. 7. In the CeVTi sample, the peaks at 489 °C and 545 °C are attributed to the reduction of nonstoichiometric V<sup>5+</sup> and Ce<sup>4+</sup> in the surface region, respectively.<sup>11,50–53</sup> The peaks at 385 °C and 397 °C of FeCeVTi samples are attributed to the reduction of Fe<sub>2</sub>O<sub>3</sub> → Fe<sub>3</sub>O<sub>4</sub> and the presence of Fe<sup>3+</sup> has been proved by XPS. The peaks at 440 °C and 445 °C are attributed to the overlap of the reduction peaks of V<sup>5+</sup> and Fe<sub>3</sub>O<sub>4</sub> → FeO.<sup>48,54</sup> With increasing Fe content, the reduction peaks of V<sup>5+</sup> and Ce<sup>4+</sup> shifted to lower temperature, which further indicated the probable interaction between Fe, Ce and V combined with the XPS result. For MnCeVTi samples, the peak at 386 °C could be attributed to the overlapping of MnO<sub>2</sub> to Mn<sub>2</sub>O<sub>3</sub> and Mn<sub>2</sub>O<sub>3</sub> to Mn<sub>3</sub>O<sub>4</sub> reduction peaks, and the peak at 447 °C may be attributed to the reduction of Mn<sub>3</sub>O<sub>4</sub> to MnO.<sup>52,55</sup> No obvious shift of the ceria reduction

**Fig. 7** H<sub>2</sub>-TPR profiles of the prepared catalysts.

peak was observed in MnCeVTi samples. Based on the results of XRD, Raman, XPS and TPR, the added Fe may exist as  $\text{Fe}_2\text{O}_3$  and  $\text{FeVO}_x$  phases in FeCeVTi catalysts and the added Mn may exist in  $\text{Mn}_2\text{O}_3$  and  $\text{MnO}_2$  phases in MnCeVTi catalysts. Ce and V may form  $\text{CeO}_2$  and  $\text{V}_2\text{O}_5$  phases in all the prepared catalysts. These oxides were highly dispersed on the surface of  $\text{TiO}_2$ .

The onset of reduction temperature for CeVTi was observed at 407 °C. With increasing amount of Fe or Mn, the onset temperature decreased gradually. This indicated a synergistic effect between the ceria-titania matrix and the incorporated Fe or Mn species.<sup>52</sup> The  $\text{H}_2$  consumption increased with increasing content of Fe or Mn, indicating more active sites on FeCeVTi and MnCeVTi samples than the CeVTi sample. The sequence of the onset of reduction temperature for these samples was:  $x\%\text{MnCeVTi}$  catalyst <  $x\%\text{FeCeVTi}$  catalyst < CeVTi catalyst. Although the highest redox ability of the  $x\%\text{MnCeVTi}$  catalyst contributed to its high  $\text{NH}_3$ -SCR activity at low temperature, it resulted in unselective oxidation of  $\text{NH}_3$  and low  $\text{N}_2$  selectivity (Fig. 1). It also may decrease the  $\text{NH}_3$ -SCR activity at temperatures above 235 °C due to the oxidation of NO to  $\text{NO}_2$ . Therefore, the  $x\%\text{FeCeVTi}$  catalyst showed a higher redox ability than the CeVTi catalyst, translating to a higher  $\text{NH}_3$ -SCR activity at low temperature. Moreover, the moderate redox ability of the  $x\%\text{FeCeVTi}$  catalyst made it maintain the high  $\text{N}_2$  selectivity.

**3.3.3 Variation of  $\text{NH}_3/\text{NO}$  adsorption ability.** It is well recognized that the adsorption and activation of  $\text{NH}_3$  played an important role in the  $\text{NH}_3$ -SCR reaction, which was greatly dependent on the surface acidity of the SCR catalyst.<sup>56</sup>  $\text{NH}_3$ -TPD results indicate the amount and strength of acid sites on the catalysts. As shown in Fig. 8a, the bands below 200 °C are generally ascribed to weakly adsorbed  $\text{NH}_3$  and therefore are excluded when discussing surface acidity. The band in the range of 200–350 °C and that above 350 °C are due to the desorption of  $\text{NH}_3$  on the medium strength and strong acidic sites, respectively.<sup>57,58</sup> The  $\text{NH}_3$  desorption peaks of MnCeVTi catalysts centered at ca. 285 °C were mainly caused by the desorption of  $\text{NH}_3$  on the weak and medium strength acid sites, and the main peak heights of MnCeVTi catalysts increased with the ratio of Mn. The  $\text{NH}_3$  desorption peaks of CeVTi and FeCeVTi catalysts centered at ca. 335 °C were due to the desorption of  $\text{NH}_3$  on the medium strength and strong acid sites. 7%FeCeVTi and CeVTi catalysts had the most acid sites among the seven catalysts in the temperature range of 290–385 °C and 385–500 °C, respectively. Compared with the CeVTi sample, the edges of  $\text{NH}_3$  desorption peaks for FeCeVTi and MnCeVTi samples shifted to lower temperature with the increase of Fe or Mn content. The MnCeVTi catalysts shifted to lower temperature than the FeCeVTi catalysts. The introduction of Mn into the CeVTi system obviously increased a part of medium strength acid sites, and decreased the strong acid sites. The introduction of Fe increased the medium strength acid sites and a part of strong acid sites. The change of acid sites was in accordance with the variation of SCR activity of these catalysts.

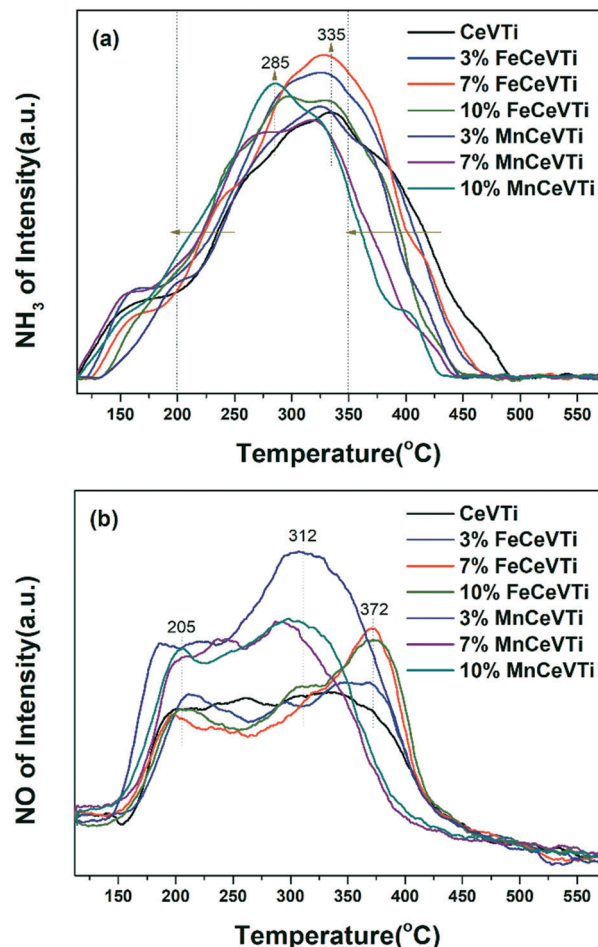


Fig. 8 (a)  $\text{NH}_3$ -TPD and (b) NO-TPD profiles of the prepared catalysts.

NO-TPD characterization was also performed to investigate the chemical adsorption of NO on the catalysts. As shown in Fig. 8b, the NO desorption pattern recorded for the MnCeVTi and FeCeVTi samples consisted of three bands centered at about 205, 312 and 372 °C. The band at 205 °C was due to the weakly chemisorbed NO. The peaks at 312 and 372 °C were caused by thermal decomposition of surface nitrates. In the SCR reaction, some surface nitrates may decompose to  $\text{N}_2\text{O}$ .<sup>59</sup> Compared with the CeVTi catalyst, the shift to lower temperature for the NO desorption peak was observed in MnCeVTi samples, especially in 7%MnCeVTi, which indicated that the decomposition of surface nitrates on them was easier. This may be one of the reasons for their high  $\text{N}_2\text{O}$  production in the activity test. FeCeVTi samples had a similar temperature range to CeVTi, which may be the reason for the addition of Fe having little effect on  $\text{N}_2$  selectivity. But the intensity of the peak at 372 °C increases with Fe content, indicating that the amount of NO adsorption on FeCeVTi samples was higher than that on CeVTi, which may result in increasing  $\text{N}_2\text{O}$  production to some degree.<sup>60</sup>

DRIFTS is a versatile tool to get information about the nature of adsorbed species on the surface of the catalyst. As shown in Fig. 9a, after 500 ppm  $\text{NH}_3$  adsorption for 30 min



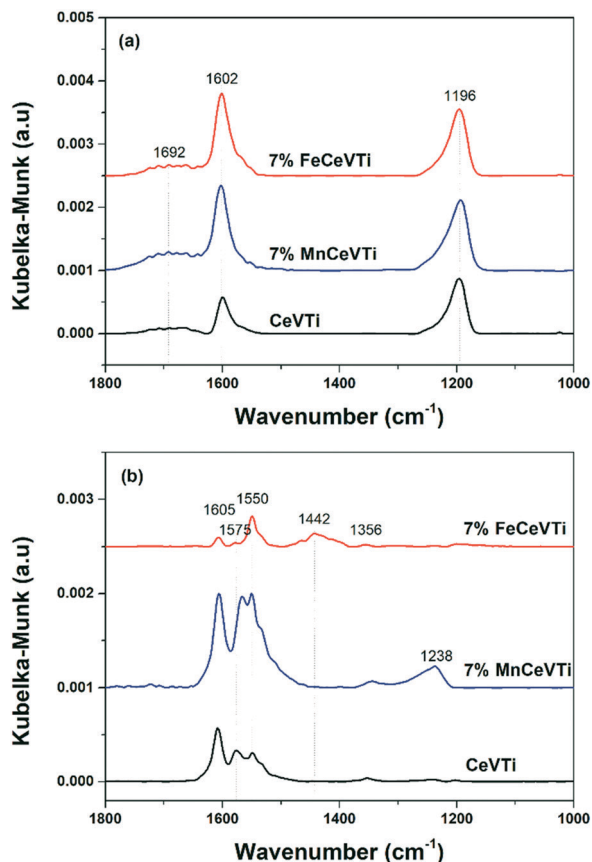


Fig. 9 DRIFTS of the prepared catalysts exposed to (a) 500 ppm NH<sub>3</sub>/N<sub>2</sub> and (b) 500 ppm NO + 5% O<sub>2</sub>/N<sub>2</sub> for 30 min followed by 20 min of N<sub>2</sub> purge at 250 °C.

and N<sub>2</sub> purge for 20 min, infrared bands characteristic of NH<sub>3</sub> adsorbed species over the samples were observed, including the NH<sub>4</sub><sup>+</sup> species on Brønsted acid sites at 1692 cm<sup>-1</sup> due to the symmetric bending vibration, and the coordinated NH<sub>3</sub> species on Lewis acid sites at 1602 and 1196 cm<sup>-1</sup> due to asymmetric and symmetric deformation vibrations of the N–H bonds, respectively.<sup>13,31,61,62</sup> The types of surface acid sites on the three samples were similar and most of them were Lewis acid sites. The addition of Fe or Mn increased the amount of acid sites. As seen from Fig. 9b, after 500 ppm NO + 5% O<sub>2</sub> adsorption and N<sub>2</sub> purge, the infrared bands attributed to monodentate nitrate (1550, 1442 and 1238 cm<sup>-1</sup>), bidentate nitrate (1605 and 1575 cm<sup>-1</sup>) and nitrates (NO<sub>3</sub><sup>-</sup>) at 1356 cm<sup>-1</sup> were observed.<sup>31,48,61</sup> The bands at 1442 cm<sup>-1</sup> and 1238 cm<sup>-1</sup> were clearly observed on 7%FeCeVTi and 7%MnCeVTi, respectively. The added Mn increased the adsorbed NO<sub>x</sub> species at 250 °C.

### 3.4 NH<sub>3</sub>-SCR reaction mechanism

Our previous study indicated the possible co-existence of both E–R and L–H reaction mechanisms in the SCR reaction on the MnCeVTi catalyst (Mn/Ti molar ratio was 40%).<sup>25</sup> To explore the NH<sub>3</sub>-SCR reaction mechanism over the optimized

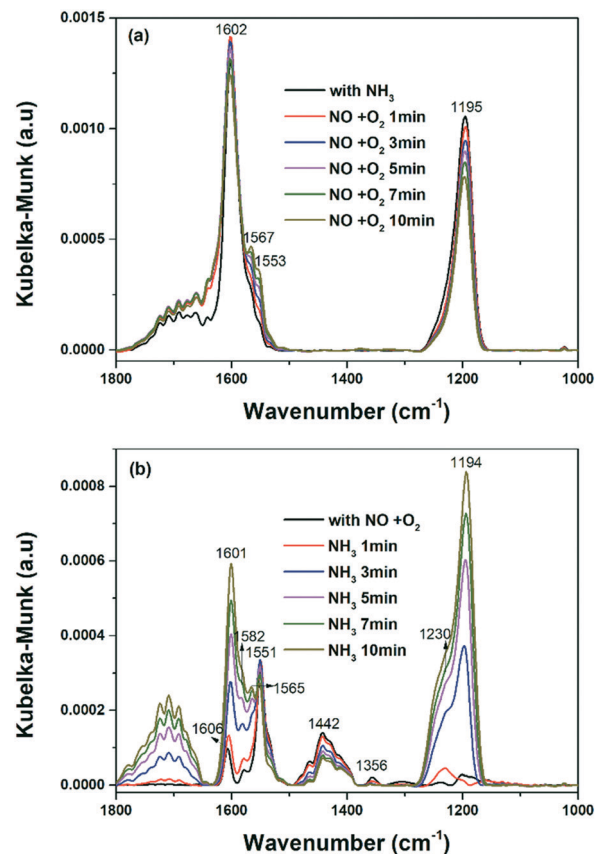


Fig. 10 *In situ* DRIFTS of the 7%FeCeVTi catalyst exposed to (a) 500 ppm NO + 5% O<sub>2</sub>/N<sub>2</sub> after 500 ppm NH<sub>3</sub>/N<sub>2</sub> for 30 min followed by 20 min of N<sub>2</sub> purge, and (b) 500 ppm NH<sub>3</sub>/N<sub>2</sub> after 500 ppm NO + 5% O<sub>2</sub>/N<sub>2</sub> for 30 min followed by 20 min of N<sub>2</sub> purge in order at 250 °C.

7%FeCeVTi catalyst, *in situ* DRIFTS analysis of the reaction between NH<sub>3</sub> and NO + O<sub>2</sub> was conducted. The 7%FeCeVTi catalyst was firstly adsorbed with NH<sub>3</sub>/N<sub>2</sub> for 30 min and then purged with N<sub>2</sub> for 20 min. When NO + O<sub>2</sub> was introduced into the reaction chamber, the spectra were recorded as a function of time at 250 °C and the results are shown in Fig. 10a. The band at 1195 cm<sup>-1</sup> of adsorbed NH<sub>3</sub> species gradually decreased with time after the introduction of NO + O<sub>2</sub>. On the other hand, the band at 1602 cm<sup>-1</sup> increased after the introduction of NO + O<sub>2</sub> for 1 min due to the overlap of the bands of adsorbed NH<sub>3</sub> species and NO<sub>x</sub> and then decreased with time due to the consumption of NH<sub>3</sub> species. This process indicated the probable presence of the Eley–Rideal (E–R) mechanism on the 7%FeCeVTi catalyst, in which the adsorbed NH<sub>3</sub> species on acid sites react with gaseous NO to form N<sub>2</sub> and H<sub>2</sub>O. Meanwhile, several bands of adsorbed NO<sub>x</sub> (1567 and 1553 cm<sup>-1</sup>) formed and increased with time.

To further understand the reaction mechanism, the process in the reverse order was also conducted and the results are shown in Fig. 10b. That is, the catalyst was firstly pre-adsorbed with NO + O<sub>2</sub> and then NH<sub>3</sub> was introduced into the reactor. As shown in Fig. 10b, the bands at 1551 and 1442 cm<sup>-1</sup> of adsorbed NO<sub>x</sub> species decreased gradually after

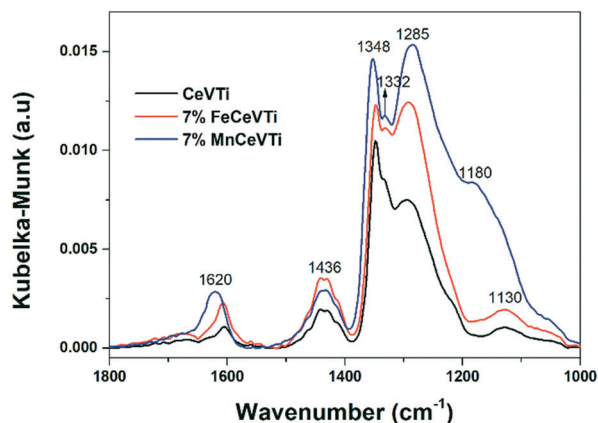


Fig. 11 *In situ* DRIFTS of CeVTi, 7%FeCeVTi and 7%MnCeVTi catalysts exposed to 500 ppm SO<sub>2</sub> + 5% O<sub>2</sub>/N<sub>2</sub> for 30 min after 500 ppm NH<sub>3</sub> and 500 ppm NO + 5% O<sub>2</sub>/N<sub>2</sub> for 30 min followed by 20 min of N<sub>2</sub> purge at 250 °C.

the introduction of NH<sub>3</sub>. This indicated the possible existence of the Langmuir–Hinshelwood (L–H) mechanism, in which adsorbed NO could react with adsorbed NH<sub>3</sub>. Meanwhile, several bands of adsorbed NH<sub>3</sub> species (1800–1635, 1601, 1230 and 1194 cm<sup>-1</sup>) formed and increased with time. As shown in Fig. S6,<sup>†</sup> the consumption of adsorbed NH<sub>3</sub> species was observed after the introduction of NO + O<sub>2</sub> and consumption of adsorbed NO<sub>x</sub> species was not observed on the CeVTi catalyst. The NH<sub>3</sub>-SCR reaction on the CeVTi catalyst followed the E–R mechanism, and the addition of Fe showed the coexistence of E–R and L–H mechanisms on the 7%FeCeVTi catalyst.

After the three catalysts were pre-adsorbed with 500 ppm NH<sub>3</sub> + 500 ppm NO + 5% O<sub>2</sub>/N<sub>2</sub> for 30 min followed by 20 min of N<sub>2</sub> purge, they were exposed to 500 ppm SO<sub>2</sub> + 5% O<sub>2</sub>/N<sub>2</sub> for 30 min and several new bands at 1436, 1348, 1332, 1285, 1180 and 1130 cm<sup>-1</sup> appeared (Fig. 11). They were attributed to the stretching motion of adsorbed sulfate species on the surface of the catalyst. Besides, the band at 1620 cm<sup>-1</sup> was assigned to adsorbed H<sub>2</sub>O due to the reaction of SO<sub>2</sub> and surface hydroxyl groups.<sup>61,63</sup> The major difference was the intensity of these bands on the three catalysts, indicating that a lower amount of sulfur-containing species was formed in the 7%FeCeVTi catalyst than the 7%MnCeVTi catalyst. This is one reason why high SO<sub>2</sub> resistance was obtained on the 7%FeCeVTi catalyst as shown in Fig. 2.

## 4. Conclusions

In this study, a series of *x*%FeCeVTi and *x*%MnCeVTi catalysts (7.0% Ce/Ti and 1.0% V/Ti, *x*% = 3%, 7%, 10% molar ratio) were prepared and tested for NH<sub>3</sub>-SCR activity, N<sub>2</sub> selectivity and resistance to H<sub>2</sub>O and SO<sub>2</sub>. The addition of Fe increased the catalytic activity below 310 °C and resistance to SO<sub>2</sub> and H<sub>2</sub>O, and maintained 100% N<sub>2</sub> selectivity. The addition of Mn increased the catalytic activity below 235 °C, but had a large adverse effect on N<sub>2</sub> selectivity and did not contribute to

resistance to SO<sub>2</sub> and H<sub>2</sub>O. The reasons for the difference in the catalytic activity of NO<sub>x</sub> removal and N<sub>2</sub> selectivity of CeVTi, FeCeVTi and MnCeVTi catalysts were explained in four facets: first, Fe had a larger effect than Mn on the crystal phase and physical adsorption of the prepared catalysts. Second, the higher Ce<sup>3+</sup>/Ce<sup>4+</sup> and surface V<sup>5+</sup> ratio due to the interaction of Fe, Ce and V in the FeCeVTi catalyst than that in the MnCeVTi catalyst contributed to the catalytic activity of the FeCeVTi catalyst at high temperatures above 235 °C. Third, the appropriate redox ability of FeCeVTi catalysts contributed to their higher NH<sub>3</sub>-SCR activity than the CeVTi catalyst at low temperature while maintaining the high N<sub>2</sub> selectivity. Although the high redox ability of MnCeVTi catalysts contributed to their high activity at low temperature, it resulted in unselective oxidation of NH<sub>3</sub> relating to low N<sub>2</sub> selectivity and oxidation from NO to NO<sub>2</sub> relating to decreasing activity above 235 °C. Four, addition of FeO<sub>x</sub> into the CeVTi system increased the medium strength acid sites and a part of strong acid sites, while MnO<sub>x</sub> increased a part of medium strength acid sites and decreased the strong acid sites.

Based on the *in situ* DRIFTS study, the addition of Fe and Mn both increased the amount of acid sites which mostly were Lewis acid sites at 250 °C. The NH<sub>3</sub>-SCR reaction on the CeVTi catalyst follows the E–R mechanism, and the addition of Fe or Mn shows the coexistence of E–R and L–H mechanisms on the catalysts. The increased amount of acid sites and decreased formation rate of sulfur-containing species on the 7%FeCeVTi catalyst contributed to the highest resistance to SO<sub>2</sub>.

## Author contributions

Conceptualization: Jinxiu Wang; methodology: Jinxiu Wang and Zongli Xie; formal analysis and investigation: Jinxiu Wang, Xianfang Yi and Qingfa Su; writing – original draft preparation: Jinxiu Wang; writing – review and editing: Zongli Xie; supervision: Jinsheng Chen and Zongli Xie.

## Conflicts of interest

There are no conflicts to declare.

## Acknowledgements

This work is financially supported by Fujian Provincial Department of Science and Technology, China [2020Y0085] and Youth Innovation Promotion Association, Chinese Academy of Sciences [2020309]. J. Wang acknowledges the scholarship from the China Scholarship Council (CSC) visiting scholar program.

## References

- 1 G. Busca, L. Lietti, G. Ramis and F. Berti, *Appl. Catal., B*, 1998, **18**, 1–36.
- 2 J. Li, H. Chang, L. Ma, J. Hao and R. T. Yang, *Catal. Today*, 2011, **175**, 147–156.

- 3 M. Fu, C. Li, P. Lu, L. Qu, M. Zhang, Y. Zhou, M. Yu and Y. Fang, *Catal. Sci. Technol.*, 2014, **4**, 14–25.
- 4 H. Jung, E. Park, M. Kim and J. Jurng, *Waste Manage.*, 2017, **61**, 283–287.
- 5 J. Xu, G. Chen, F. Guo and J. Xie, *Chem. Eng. J.*, 2018, **353**, 507–518.
- 6 C. Chen, Y. Cao, S. Liu, J. Chen and W. Jia, *Chin. J. Catal.*, 2018, **39**, 1347–1365.
- 7 L. Han, S. Cai, M. Gao, J.-y. Hasegawa, P. Wang, J. Zhang, L. Shi and D. Zhang, *Chem. Rev.*, 2019, **119**, 10916–10976.
- 8 Y. Yang, W. Xu, J. Wang and T. Zhu, *Fuel*, 2019, **249**, 178–187.
- 9 J. Arfaoui, A. Ghorbel, C. Petitto and G. Delahay, *Appl. Catal., B*, 2018, **224**, 264–275.
- 10 W. Cha, S. H. Ehrman and J. Jurng, *Chem. Eng. J.*, 2016, **304**, 72–78.
- 11 W. Cha, S. H. Ehrman and J. Jurng, *J. Environ. Chem. Eng.*, 2016, **4**, 556–563.
- 12 X. Zhang, C. Li, L. Zhao, J. Zhang, G. Zeng, Y. E. Xie and M. E. Yu, *Appl. Surf. Sci.*, 2015, **347**, 392–400.
- 13 Z. Liu, S. Zhang, J. Li, J. Zhu and L. Ma, *Appl. Catal., B*, 2014, **158–159**, 11–19.
- 14 K. J. Lee, P. A. Kumar, M. S. Maqbool, K. N. Rao, K. H. Song and H. P. Ha, *Appl. Catal., B*, 2013, **142–143**, 705–717.
- 15 S. Chen, M. A. Vasiliades, Q. Yan, G. Yang, X. Du, C. Zhang, Y. Li, T. Zhu, Q. Wang and A. M. Efstathiou, *Appl. Catal., B*, 2020, **277**, 119186.
- 16 C. Gao, J. W. Shi, Z. Fan, G. Gao and C. Niu, *Catalysts*, 2018, **8**, 11–39.
- 17 C. Liu, J. W. Shi, C. Gao and C. Niu, *Appl. Catal., A*, 2016, **522**, 54–69.
- 18 N. Husnain, E. Wang, K. Li, M. T. Anwar, A. Mehmood, M. Gul, D. Li and J. Mao, *Rev. Chem. Eng.*, 2019, **35**, 239–264.
- 19 W. Shan and H. Song, *Catal. Sci. Technol.*, 2015, **5**, 4280–4288.
- 20 Z. Wu, R. Jin, Y. Liu and H. Wang, *Catal. Commun.*, 2008, **9**, 2217–2220.
- 21 F. Wang, B. Shen, S. Zhu and Z. Wang, *Fuel*, 2019, **249**, 54–60.
- 22 J. Tian, K. Zhang, W. Wang, F. Wang, J. Dan, S. Yang, J. Zhang, B. Dai and F. Yu, *Green Energy & Environment*, 2019, **4**, 311–321.
- 23 K. B. Nam, D. H. Kim and S. C. Hong, *Appl. Catal., A*, 2019, **572**, 107–114.
- 24 Y. Niu, T. Shang, S. Hui, X. Zhang, Y. Lei, Y. Lv and S. Wang, *Fuel*, 2016, **185**, 316–322.
- 25 J. Wang, X. Yi, D. Ng, H. Li, J. Miao, Q. Su, J. Chen and Z. Xie, *Top. Catal.*, 2020, **63**, 913–923.
- 26 X. Zhao, L. Mao and G. Dong, *Catalysts*, 2018, **8**, 76–89.
- 27 L. Schill, S. S. R. Putluru, A. D. Jensen and R. Fehrmann, *Catal. Commun.*, 2014, **56**, 110–114.
- 28 N. Zhu, W. Shan, Z. Lian, Y. Zhang, K. Liu and H. He, *J. Hazard. Mater.*, 2020, **382**, 120970.
- 29 S. Xiong, Y. Liao, X. Xiao, H. Dang and S. Yang, *J. Phys. Chem. C*, 2015, **119**, 4180–4187.
- 30 S. Raja, M. S. Alphin and L. Sivachandiran, *Catal. Sci. Technol.*, 2020, **10**, 7795–7813.
- 31 T. H. Vuong, J. Radnik, J. Rabeah, U. Bentrup, M. Schneider, H. Atia, U. Armbruster, W. Grünert and A. Brückner, *ACS Catal.*, 2017, **7**, 1693–1705.
- 32 M. T. Van Dongen, D. Ng, L. V. Moura, D. Acharya, J. Wang, C. D. Easton, F. Wang and Z. Xie, *J. Chem. Technol. Biotechnol.*, 2020, DOI: 10.1002/jctb.6612.
- 33 J. G. Yu, L. J. Zhang, B. Cheng and Y. R. Su, *J. Phys. Chem. C*, 2007, **111**, 10582–10589.
- 34 J. Liu, X. Li, Q. Zhao and D. Zhang, *Catal. Sci. Technol.*, 2012, **2**, 1711–1718.
- 35 P. C. J. Graat and M. A. J. Somers, *Appl. Surf. Sci.*, 1996, **100–101**, 36–40.
- 36 V. Di Castro and G. Polzonetti, *J. Electron Spectrosc. Relat. Phenom.*, 1989, **48**, 117–123.
- 37 H. W. Nesbitt and D. Banerjee, *Am. Mineral.*, 1998, **83**, 305–315.
- 38 M. Romeo, K. Bak, J. El Fallah, F. Le Normand and L. Hilaire, *Surf. Interface Anal.*, 1993, **20**, 508–512.
- 39 E. Bêche, P. Charvin, D. Perarnau, S. Abanades and G. Flamant, *Surf. Interface Anal.*, 2008, **40**, 264–267.
- 40 Z. Liu, H. Liu, H. Zeng and Q. Xu, *Catal. Sci. Technol.*, 2016, **6**, 8063–8071.
- 41 L. Kang, L. Han, J. He, H. Li, T. Yan, G. Chen, J. Zhang, L. Shi and D. Zhang, *Environ. Sci. Technol.*, 2019, **53**, 938–945.
- 42 K. Tsuji and I. Shiraishi, *Fuel*, 1997, **76**, 549–553.
- 43 F. Liu, H. He, Z. Lian, W. Shan, L. Xie, K. Asakura, W. Yang and H. Deng, *J. Catal.*, 2013, **307**, 340–351.
- 44 N. Kruse and S. Chenakin, *Appl. Catal., A*, 2011, **391**, 367–376.
- 45 Z. Jiang, D. Ding, L. Wang, Y. Zhang and L. Zan, *Catal. Sci. Technol.*, 2017, **7**, 3065–3072.
- 46 K. Lee, M. Maqbool, A. Pullur, Y. Jeong, K. Song and H. Ha, *Res. Chem. Intermed.*, 2015, **41**, 2635–2650.
- 47 Y. K. Yu, C. He, J. S. Chen and X. R. Meng, *J. Fuel Chem. Technol.*, 2012, **40**, 1359–1365.
- 48 F. Liu, W. Shan, Z. Lian, J. Liu and H. He, *Appl. Catal., B*, 2018, **230**, 165–176.
- 49 F. Liu, K. Asakura, H. He, W. Shan, X. Shi and C. Zhang, *Appl. Catal., B*, 2011, **103**, 369–377.
- 50 H. Zhao, S. Bennici, J. Shen and A. Auroux, *J. Catal.*, 2010, **272**, 176–189.
- 51 V. Perrichon, A. Laachir, G. Bergeret, R. Fréty, L. Tournayan and O. Touret, *J. Chem. Soc., Faraday Trans.*, 1994, **90**, 773–781.
- 52 B. Murugan and A. V. Ramaswamy, *J. Phys. Chem. C*, 2008, **112**, 20429–20442.
- 53 K. Cheng, W. Song, Y. Cheng, J. Liu, Z. Zhao and Y. Wei, *Catal. Sci. Technol.*, 2016, **6**, 4478–4490.
- 54 S. Yua, D. Guojun, Z. Yuanb, Z. Yufengb and W. Yajieb, *Indian J. Chem.*, 2015, **54**, 744–751.
- 55 X. Tian, B. Lin, Y. Li, S. Wang, Y. Zhou and H. Zhong, *Catal. Sci. Technol.*, 2020, **10**, 4553–4561.
- 56 S. X. Wang, R. T. Guo, W. G. Pan, M. Y. Li, P. Sun, S. M. Liu, S. W. Liu, X. Sun and J. Liu, *Phys. Chem. Chem. Phys.*, 2017, **19**, 5333–5342.
- 57 Q. Xu, R. Su, L. Cao, Y. Li, C. Yang, Y. Luo, J. Street, P. Jiao and L. Cai, *RSC Adv.*, 2017, **7**, 48785–48792.
- 58 Y. Yu, J. Miao, J. Wang, C. He and J. Chen, *Catal. Sci. Technol.*, 2017, **7**, 1590–1601.
- 59 S. Yang, S. Xiong, Y. Liao, X. Xiao, F. Qi, Y. Peng, Y. Fu, W. Shan and J. Li, *Environ. Sci. Technol.*, 2014, **48**, 10354–10362.

- 60 L. Chmielarz, P. Kuśtrowski, M. Zbroja, W. Łasocha and R. Dziembaj, *Catal. Today*, 2004, **90**, 43–49.
- 61 Y. Yu, J. Wang, J. Chen, X. Meng, Y. Chen and C. He, *Ind. Eng. Chem. Res.*, 2014, **53**, 16229–16234.
- 62 N. Y. Topsoe, H. Topsoe and J. A. Dumesic, *J. Catal.*, 1995, **151**, 226–240.
- 63 L. Zhao, X. Li, C. Hao and C. L. Raston, *Appl. Catal., B*, 2012, **117–118**, 339–345.